## NASA DEVELOP National Program Virginia – Langley

Fall 2024

# Chile Metropolitan Region Disasters

Enhancing Authority Response to Storm Floods in Chile Leveraging Automatic Satellite Image Processing

## **DEVELOP** Technical Report

November 22<sup>nd</sup>, 2024

Isabella Giordano, Analytical Mechanics Associates (Project Lead) Viviana Bravo Ortiz, Analytical Mechanics Associates Jackie Encinas, Analytical Mechanics Associates Patrick O'Shea, Analytical Mechanics Associates

#### Advisors:

Dr. Kenton Ross, NASA Langley Research Center (Science Advisor) Dr. Xia Cai, NASA Langley Research Center (Science Advisor)

#### Lead:

Alyson Bergamini (Virginia – Langley)

#### 1. Abstract

The Metropolitan Region in central Chile is home to approximately 7 million people. The region frequently experiences disastrous floods, physically impacting tens of thousands of people and causing millions of dollars in damage. Remote sensing methods used to map flooding extents can help emergency responders allocate resources efficiently. Partnering with Centro de Información de Recursos Naturales (CIREN) in collaboration with the Embassy of Chile Agricultural Office, we leveraged the use of satellites Landsat 8 Operational Land Imager (OLI), Landsat 9 OLI-2, Sentinel-1 Synthetic Aperture Radar (SAR) and Sentinel-2 Multispectral Instrument (MSI) and hydraulic modeling to resolve flood extents for recent January 29, 2021, and August 23, 2023 flood events. Compared to a reported August 2023 flooding extents, we found that the Earth observation and hydraulic modeling results were significantly less extensive. Additionally, we found that optical and radar datasets were inconsistent means of capturing flood extents, while hydraulic modeling incorporating discharge observations from stream gauges provides a more reliable tool for modeling future flood impacts within the Chile Metropolitan Region. The addition of more localized parameters by CIREN in the hydraulic model can further enhance the model's outputs. With these results, CIREN can integrate hydraulic modeling into their current methods to characterize riverine floods. While optical and radar imagery are feasible, CIREN should consider their limitations, given issues with cloud contaminations, data quality and temporal restraints.

## **Key Terms**

remote sensing, flood susceptibility, Chile, Landsat 8 OLI, Sentinel-1 SAR, Sentinel-2 MSI, HEC-RAS

#### 2. Introduction

## 2.1 Background information

Chile has a long history of disastrous floods dating back to the late 16th century (Rojas et al., 2014). Several factors lead to Chile's flood-prone nature including the country's climatic conditions, topographic & tectonic settings, and recent urbanization (Ebert et al., 2010; Gironás et al., 2021; Krellenberg et al., 2013; Rojas et al., 2014). Evidence suggests that future development combined with climate change will impact the frequency and severity of flooding events (Ebert et al., 2009; Krellenberg et al., 2013; Vicuna et al., 2013). These factors have culminated in Chile experiencing losses due to natural disasters that equate to 1.2% of the country's annual GDP every year between 1980 and 2011 and landing the country in the top 30 countries that are under the highest water-related risk by 2025 (Gironás et al., 2021; Luo et al., 2015). As the risk of flooding intensifies in Chile, disaster response personnel must be equipped to quickly and accurately map flooding patterns to help expedite disaster relief efforts.

The Metropolitan Region, centrally located within Chile and containing the capital of Santiago, is frequently impacted by flooding (Figure 1). The Region encompasses 15,403 kilometers², is topographically bound by the Central Andeans and Costal Cordilleras to the east and west and is home to around 7 million residents (Ebert et al., 2010; Krellenberg et al., 2013). The Maipo and Mapocho Rivers traverse the Region from east to west, ultimately terminating in the Pacific Ocean. The Rapel River borders the Metropolitan Region and Libertador General Bernardo O'Higgins Region to the south. Both rivers had notable flooding events occur in June 2023. This event made headlines when the most intense rainfall event recorded in the last 30 years unleashed a deluge of flooding upon several regions, physically impacting nearly 21,000 people and causing significant damage to critical infrastructure (IFRC, 2024; Olivares et al., 2023). Eight weeks later, a second major flood displaced over 30,000 residents (Davies, 2023). Most recently, in June 2024, local reports indicate that nearly 2,000 homes in the Metropolitan Region were damaged, with 60,000 people losing power (Deutsche Welle, 2024).

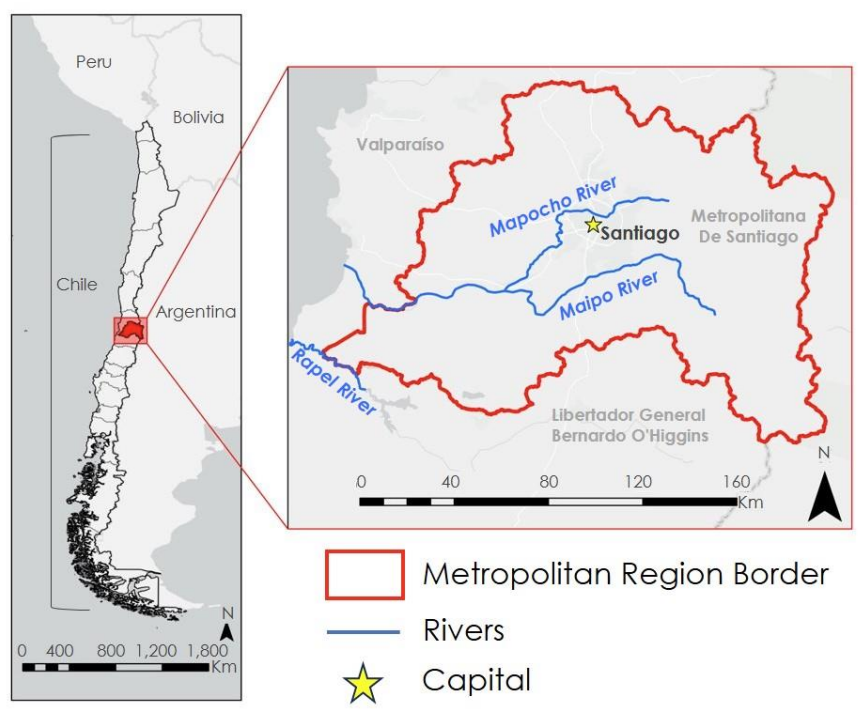


Figure 1. Map of Santiago Metropolitan Region, Chile, including the Maipo, Mapocho, and Rapel Rivers. Basemap credits: Esri, TomTom, Garmin, FAO, NOAA, USGS

Remote sensing and conventional hydraulic models are frequently used to assess flooding. Satellites equipped with sensors can obtain measurements covering large spatial scales, aiding emergency responders in understanding a disaster's magnitude and assessing affected areas across a region (Melancon et al., 2021). Previous research have used optical and radar-based Earth observations to assess flood patterns. Ban et al. (2017) used Terra Moderate Resolution Imaging Spectroradiometer visible and near-infrared bands to map flooding in the Philippines and China in 2015 and 2016. Melancon et al. (2021) used Sentinel-1 Synthetic Aperture Radar (SAR) data in a random-forest classification model to map flooding across North and South Carolina following Hurricane Florence. Both studies showed how useful Earth Observations can be for mapping inundated areas, but they also highlight the need for higher spatial-temporal resolutions and validation data to assess accuracy. Other studies analyzed flood vulnerability indicators, such as urban growth patterns, land use change, and vegetation loss using remote sensing datasets (Krellenberg et al., 2013). Satellite imagery coupled with the hydrological model, Hydrologic Engineering Center – Hydrologic Modeling System (HEC-HMS), allowed Ebert et al. (2009) to analyze how urban growth influences hydrology and flood hazard in Santiago. Previous DEVELOP teams have explored rapid flood detection tools such as HYDRAFloods (Hietpas et al., 2021) and Open Data Cube (Casey et al., 2022) to map flood extent.

## 2.2 Project Partners and Objectives

We partnered with Centro de Información de Recursos Naturales (CIREN) in collaboration with the Embassy of Chile's Agricultural Office. CIREN supports Chile's Ministry of Agriculture to aid in managing the country's natural resources. CIREN staff are experienced with remote sensing technologies, and they collect information through geospatial applications to create a comprehensive, georeferenced database of natural resources. They also provide other organizations with information on potential environmental risks, climate change, natural disasters, and mitigation techniques.

As flooding disasters affect natural resources, CIREN is seeking a monitoring technique to predict floods and map regions susceptible to flood damage. Determining if hydraulic modeling or Earth observations (EOs) are feasible to map floods in Chile will allow our partners to decide if NASA or European Space Agency (ESA)

imagery should be added to their current toolbox. Added results will enhance CIREN's efforts to conserve and protect natural resources from flood hazards. In addition, CIREN's stakeholders, which include researchers, agricultural producers, and public institutions, are not as familiar with remote sensing, so a clear workflow and non-code method would help CIREN share our results with their users.

The objectives of our project include: 1) estimate flood extent in the study area using a hydraulic model, 2) identify flooded areas using optical and radar data and 3) assess the feasibility of these methods to map flood extent in the Region. We based our project on three major flooding events in the Region: January 29, 2021, June 23, 2023, and August 23, 2023, as these events were based on personal recounts from our partners and news articles. Focusing on data from recent flooding disasters would support CIREN's current decision-making needs for disaster relief programs.

## 3. Methodology

#### 3.1 Data Acquisition

#### 3.1.1 Hydraulic Engineering Center – River Analysis System (HEC-RAS)

We used the River Analysis System from the Hydrologic Engineering Center, a division within the US Army Corp of Engineers. This model, more commonly known as HEC-RAS, allows users to create two-dimensional (2-D) hydraulic models of a flood event. To construct our 2-D model, we derived several model characteristics from outside data sources, including the discharge rates associated with the flood and the topographic and land use data associated with areas where flooding occurred. We obtained 15-minute and daily average discharge data from CIREN from their internal stream gauge network. Of the 35 stream gauges provided, we focused on stream gauges 05710012-5 and 05710001-K, both of which are placed within the Maipo River main channel and are located approximately 1.4 kilometers downstream and 1.5 kilometers upstream of El Manzano respectively (Figure A1). By combing the records from these gauge stations, we were able to capture flooding events from January 2021, June 2023, and August 2023. It is important to note that for the June 2023 event, the gauges only captured the daily average data, given that the intense flood waters blew out both gauges between June 23 and 24. We also used 30-meter Shuttle Radar Topography Mission terrain data (NASA JPL, 2000), as well as a polygon shapefile of land cover classifications for the entire Metropolitan Region provided by CIREN.

#### 3.1.2 Radar Dataset

We obtained 10-meter Sentinel-1A C-band Synthetic Aperture Radar (C-SAR) data from the European Space Agency. NASA's Alaska Satellite Facility Distributed Active Archive Center (ASF DAAC) hosts open-access EO data products and specifically processes and distributes SAR datasets. We used ASF's Data Search Vertex portal to acquire Level – 1 Ground Range Detected (GRD) High-Resolution Dual-Polarization data. We filtered our search to the Metropolitan Region and image captured dates between January 24 – February 2, 2021, and June 12 – 27, 2023. We chose these dates to find before and after images of the January 29, 2021, and June 23, 2023 flood events. We filtered our data further to select files that were dual polarized (vertically transmitted and vertically received, or VV + VH), in ascending and descending orbit directions, and with a beam mode of Interferometric Wide. These filters resulted in images for January 26, 2021; February 1, 2021; and June 12 & 26, 2023 (Table 1).

## 3.1.3 Optical and Multispectral Datasets

We downloaded a 30-meter Landsat 8-9 Operational Land Imager (OLI)/Thermal Infrared Sensor (TIRS) Collection 2 Level 2 Science Products provided by the United States Geological Survey (USGS) through the Earth Explorer platform. We selected imagery for pre-flood (August 6) and post-flood (August 30, 2023) dates, focusing on the study area (Table 1). Additionally, we downloaded satellite images from Sentinel-2 Multispectral Instrument (MSI) Level 2A with a 10-meter spatial resolution and 32-bit Float TIFF from the ESA through Copernicus Open Access Hub. We selected the images to assess the January 29, 2021, and August 23, 2023, flood events. The images we selected for pre-flood and post-flood analysis were from January 13 and February 2, 2021, as well as August 6 and 26, 2023 (Table 1).

Table 1

Earth observations utilized for this project.

Platform and Sensors	Parameters	Processing Level	Image Capture Dates	Acquisition Methods
Landsat 8-9	Surface reflectance,	Collection 2, Level 2	August 6 and 30,	USGS Earth
OLI/TIRS	30-meter		2023	Explorer
Sentinel-1 C- SAR	Ground Range	Level 1	January 26, February	ASF DAAC Data
	Detected (GRD)		1, 2021; June 12 and	Search Vertex
	radar backscatter,		26, 2023	
	10-meter data			
Sentinel-2 MSI	Surface reflectance,	Level 2A	January 13, February	Copernicus Browser
	10-meter		2, 2021;	
			August 6 and 26,	
			2023	
Shuttle Radar	Radar backscatter,	DEM	February 11th - 20th,	NASA Earth Data
Topography	30-meters		2000	
Mission				

#### 3.2 Data Processing

#### 3.2.1 HEC-RAS

To set our processing extents, we chose a model reach along the Maipo River (Figure A2) between stream gauge 05710001-K on the upstream end and approximately 4 kilometers upstream of where Highway 79 crosses the Maipo River on the downstream end. We chose this model reach because we used flow data from 05710001-K in the model runs, as well as at the same time wanted to avoid the hydraulic control exerted by the bridge at Highway 79 on the flooding extents.

We constructed the hydraulic model using HEC-RAS v. 6.6 (U.S. Army Corps of Engineers, 2024b), which required the development of a geometry file, flow file, and plan file. We created the geometry file within RAS Mapper, a GIS interface embedded within the larger HEC-RAS model. After setting the RAS Mapper coordinate system to UTM 19 South, we converted the 30 m data from a GEOTIFF to an HDF file using RAS Mapper's terrain import workflow and brought it into the map. We used a shapefile of the study area to assign the perimeter for the geometry file. From there, we generated a regular 2-D model grid with a uniform cell size of 9.29 m². To refine the grid and align the grid cells with the river channel, we drew break lines along the river thalweg and the tops of the right and left channel overbanks. Additionally, we drew refinement regions around mountainous portions of the model and notable promontories. The uniform cells intersecting the break lines and refinement regions were both realigned and refined to smaller cell sizes to better impart the topographic complexity onto the model grid. We handled small additional grid refinements on a cell-bycell basis. This refinement effort results in a model grid comprising 31,141 cells ranging in size from nearly 1680 m² to 8.3 m², with smaller area grid cells concentrated heavily within the channel and along the right and left overbanks.

To further parameterize the geometry file, we brought the clipped land cover data into the RAS Mapper as a land cover layer. The purpose of the land cover layer is to associate the land cover classification's corresponding Manning's n value with the model grid. Manning's n is a parameter that represents the surface roughness associated with a given land cover type. These values typically range from 0.01 to 0.1, with lower values indicating smoother surfaces and higher values indicating rougher surfaces. With a smooth surface, flood water tends to flow faster and not stack as high, whereas on a rougher surface, flood water tends to instead slow down and stack higher. Manning's n values were chosen for each land cover type (Table A2). Since Manning's n values associated with each land cover type are unavailable, we obtained analog land cover types and associated them with our land cover data. Analogs were chosen using Manning's n classifications presented in Chow (1959).

Having created the geometry and flow files, we established plan files for the January 2021 and August 2023 events. Plan files are where model simulation parameters such as processing window and run tolerances are established, which, when combined with the information created in the flow and geometry files, create an entire hydraulic simulation run. To create the plan files for our flood events, we established both temporal and processing constraints. Regarding temporal constraints, we set computation windows and intervals for the January 2021 and August 2023 events (Table A1). We chose these simulation windows to provide ample buffer around the peak flows recorded by the stream gauges. In addition to setting the computation window, our team set the computation interval at five seconds. We selected this computation interval after multiple run attempts, we found it to optimize avoiding numerical instability when running our hydraulic simulation. This keeps the time for a simulation to complete within an hour. Lastly, we chose to run our hydraulic simulations using the diffusion wave approach. When using the diffusion wave approach, the conservation of momentum equation is approximated as minor terms that describe flow advection and flow turbulence. The influences of the Coriolis effect are disregarded when running the model (U.S. Army Corps of Engineers, 2024a). By disregarding these terms and electing to use the diffusion wave approach, we optimized our model run time without significant losses in model accuracy.

#### 3.2.2 Sentinel-1 SAR

Sentinel-1 GRD SAR data contains inherent geometric and radiometric distortions due to the interaction of radar signals with Earth's terrain and the side-looking angle of the sensor. We applied a radiometric terrain correction (RTC) to the SAR imagery within the ASF DAAC's Data Search Vertex Portal to overcome these distortions. The portal has a feature called On-Demand RTC, which uses cloud computing and GAMMA software to generate analysis-ready products. There are various processing options on the On-Demand RTC feature, and the ASF provides an ArcGIS Story Map as a guide when making these selections (Kristenson, 2020). First, we set the backscatter coefficient to gamma-nought, as this is the preferred setting for most GIS applications. Next, we set the scale of the backscatter output to decibels, allowing for greater differentiation among dark and light pixels. We opted to match the images to the On-Demand RTC's default GLO-30 Copernicus DEM to improve the quality of the RTC calculations. Finally, we set the pixel spacing to 10meters, as a finer-resolution provides much more surface feature details and is closer to the original spatial resolution of Sentinel-1 SAR data. After we made our RTC-processing selections, we submitted the images to the On Demand Products processing queue. Once the products were available for download, we imported the GEOTIFFs as rasters into ArcGIS Pro, version 3.3.2. We then used the Extract by Mask tool and a polygon shapefile representing a 4-mile buffer of the Maipo and Mapocho rivers to extract the raster to a focused area of interest.

#### 3.2.3 Normalized Difference Water Index from Landsat and Sentinel-2

The Normalized Difference Water Index (NDWI) is an index that helps identify water bodies, utilizing the spectral reflectance values of vegetation and water (McFeeters, 1996). It is a crucial tool for monitoring flooding (Gao, 1996). Water absorbs near-infrared light and reflects green light, resulting in higher NDWI values (>0) for water bodies and lower values (<0) for land and vegetation. We used Landsat 8-9 and Sentinel-2 imagery because their multispectral sensors provide high spatial resolution and specific spectral bands useful for NDWI calculations, particularly the green and near-infrared (NIR) bands (Masek et al., 2020). To process the images for NDWI calculation in ArcGIS Pro version 3.3.1, we created a mosaic of the images to cover the entire study area and clipped the raster to the Metropolitan Region.

Furthermore, we applied cloud and snow masking techniques to Landsat and Sentinel imagery. For the Landsat images, we used the Quality Assessment Tool from the Landsat Quality Assessment ArcGIS Toolbox (Arab et al., 2024) to identify the pixels corresponding to clouds, specifically cloud shadow, high cloud shadow confidence, dilated cloud, cloud, and snow. We then used the Extract by Mask tool to isolate the areas marked as clouds and snow from the imagery to remove potential sources of error in the NDWI calculation. For the Sentinel 2 data, we used the Scene Classification product at a 20-meter resolution, which

includes maps of cloud and snow probability and detection (Louis, 2021). We applied the Extract by Mask tool to extract these areas from the imagery.

With the Raster Calculator tool, we calculated NDWI. This index is derived using the green and the near-infrared bands from the Landsat 8-9 and Sentinel-2 imagery (Equation 1). The Raster Calculator tool generated a new raster layer that distinguished water bodies from land and vegetation.

$$NDWI = \frac{Green - NIR}{Green + NIR}$$
 (1)

### 3.3 Data Analysis

#### 3.3.1 HEC-RAS

Once our model simulations ran to completion, we extracted summary statistics, evaluated how floodplain width changed with elevation, and compared the resulting floodplain width to a reported floodplain delineation provided by CIREN. We obtained summary statistics during peak flow periods, including max discharges, max velocities, max depth, and both max and mean floodplain widths. For both evaluating floodplain width changes with elevation and comparing the model floodplain delineation against the reported delineation, we measured every 200 meters along the model reach. These measurements include the elevation and width of the modeled floodplain and reported floodplain. We then evaluated how the modeled floodplain widths compare with the reported floodplain widths and if we could discern any trends with elevation.

#### 3.3.2 Log Difference Between Backscatter Values from Sentinel-1 SAR

To analyze the flood extent of each event with SAR data, we calculated the log ratio of pixel values from the two pre- and post-flood images. We used the Calculate Log Difference Tool from the Alaskan Satellite Facility's ASF\_Tools ArcGIS Toolbox (Kennedy et al., 2024). The Calculate Log Difference Tool requires the raster inputs to be in a power scale. Since we downloaded our RTC data in decibels, we had to first use the Scale Conversion Tool from the Toolbox to convert from units of decibels to power. To calculate the log difference, we referenced the ASF's Log Difference Tool StoryMap (Kristenson, 2020). We used the vertically polarized backscatter VV band from the pre- and post-flood rasters, as this mode is best for visualizing changes in surface water due to its sensitivity to surface roughness and soil moisture.

The resulting output raster has pixels with values representing a change in backscatter over time. Positive values depict increased backscatter, while negative values represent decreased backscatter or flooding. The output raster defaults to a grayscale stretch symbology, which can be challenging to interpret. To better depict the difference, we changed the symbology of the raster to "Classify" and created five classes. We manually set the class breaks based on the dataset's standard deviations, with the values ranging from two standard deviations below and above the mean. We chose a color scheme where shades of blue represented negative values, red represented positive values, and yellow represented middle values with no change. With this updated symbology, we could see distinct color changes between the pre- and post-flood products.

#### 3.3.3 Difference in NDWI from Landsat and Sentinel-2

To detect flooding, we highlighted the changes in NDWI between the pre- and post-flood images. We used the Raster Calculator tool to subtract the post-flood water pixel values from the pre-flood water pixel values. The resulting NDWI Difference raster showed the differences in surface water after the flooding event. We applied this methodology to our processed Landsat 8-9 and Sentinel–2 data to assess water content changes during the January 2021 and August 2023 flood events. Positive values represented increased water coverage after the flood, suggesting flood-prone regions, while negative values represented areas where water coverage decreased or regions that were flooded but had dried out as the water receded.

## 4. Results

4.1 Analysis of Results

4.1.1 HEC-RAS Flood Simulation

Once we ran our HEC-RAS models for the January 29, 2021, and August 23, 2023, events, we obtained flood models that we could sample spatially and temporally within our simulation windows. For both simulations, we gathered maximum and average summary statistics for key flooding parameters, including velocity, discharge, depth, and floodplain width (Table 2). Maximum values were obtained by visualizing the peak discharge timestep within each simulation and identifying the maximum values from the associated parameter surface. The average floodplain width was obtained by averaging floodplain width measurements during the flood maximum every 200 meters (Figure A3) along the model reach. The January 29, 2021, flood event produced larger maximum values compared to the August 23, 2023, flood event (Table 3). This is driven by the maximum discharge observed for the January 2021 event being 76.6 m³/s higher than the August 2023 event. This larger January 2021 discharge, combined with the fact that the underlying model geometry did not change between model simulations, resulted in all the other flood parameters for the January 2021 event being larger than the August 2023 flood parameters.

Table 2
Hydraulic Model Simulation Summary Table

Statistic	January 29th, 2021, Simulation	August 23 <sup>rd</sup> , 2023, Simulation
Max Observed Velocity (m/s)	23.0	15.7
Max Observed Discharge (m³/s)	495.1	418.5
Max Observed Depth (m)	6.2	6.0
Max Floodplain Width (m)	185.7	119.3
Average Floodplain Width (m)	89.2	56.8

In addition to summarizing key model parameters, we also evaluated how our modeled floodplain width changed with elevation along our model reach. Understanding how floodplain width varies with elevation is a key partner concern, so we created a scatter plot showing how the model floodplain widths for January 2021 and August 2023 flood events varied along the model reach (Figure 2). The linear trend lines plotted for both models show that the floodplain width generally decreases as elevation increases. This trend is reasonable as the riparian environment of our model transitions from more of an alluvial floodplain to a more intermountain environment along the model reach. We calculated R-squared values, a measure of linear fit that varies between 0 and 1, for both trend lines and found that the R-squared values are close to 0 for both simulations. These low R-squared values indicate that the linear relationship between floodplain width and river elevation is not strong. Therefore, we can say that floodplain widths do appear to decrease with elevation, but that elevation alone is not the principal driver of this trend.

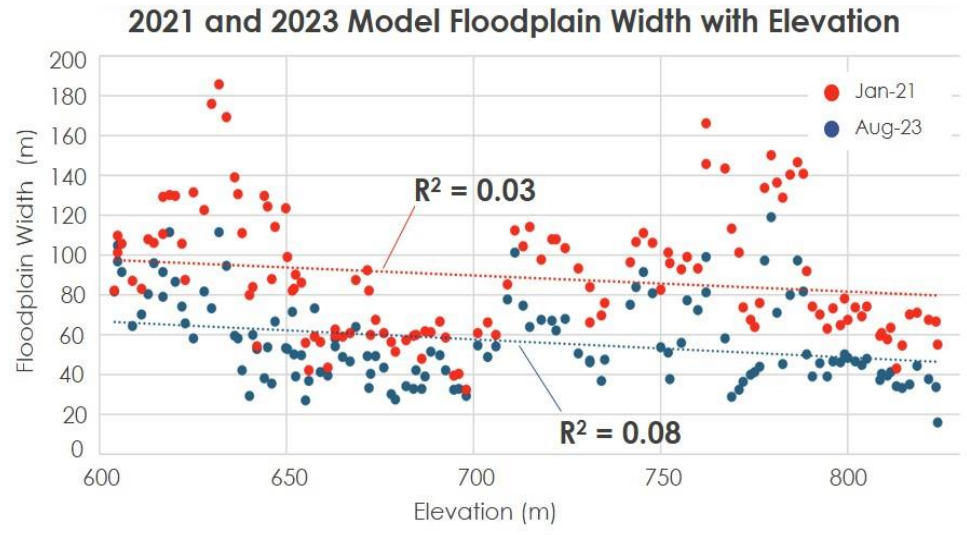


Figure 2. Scatter plot showing how floodplain width varies with elevation along the model reach for the January 29, 2021, and August 23, 2023, flooding simulations

In addition to evaluating how modeled floodplain widths varied with elevation, we also wanted to compare our model results to any reported floodplain extents for either of our storm events. CIREN provided our team with a reported floodplain extent for the August 23, 2023, flooding event, created during emergency management operations shortly after the flooding occurred. After making an initial visual comparison (Figure A4), we summarized the maximum, minimum, and average floodplain width differences at our 200-meter measuring points for both the reported and our modeled floodplain widths (Table A3). With this we found that our model significantly underpredicts the reported floodplain. Unfortunately, because the nature of how the reported floodplain was delineated was not disclosed, we could not identify why there is such a significant difference between what our model predicts and what the reported floodplain delineation suggests. Finally, we plotted our 200-meter sampled widths for the reported and modeled flooding extents against each other to better understand how the reported floodplain width varies with elevation (Figure 3). Interestingly, from its linear regression, the reported floodplain width tends to increase with elevation despite transitioning to a more mountainous riparian environment as elevation increases. However, like the modeled results, the low R-squared value of this trend means that the linear relationship fits the data poorly and that elevation alone is not the driver for the observed trends in the reported floodplain width.

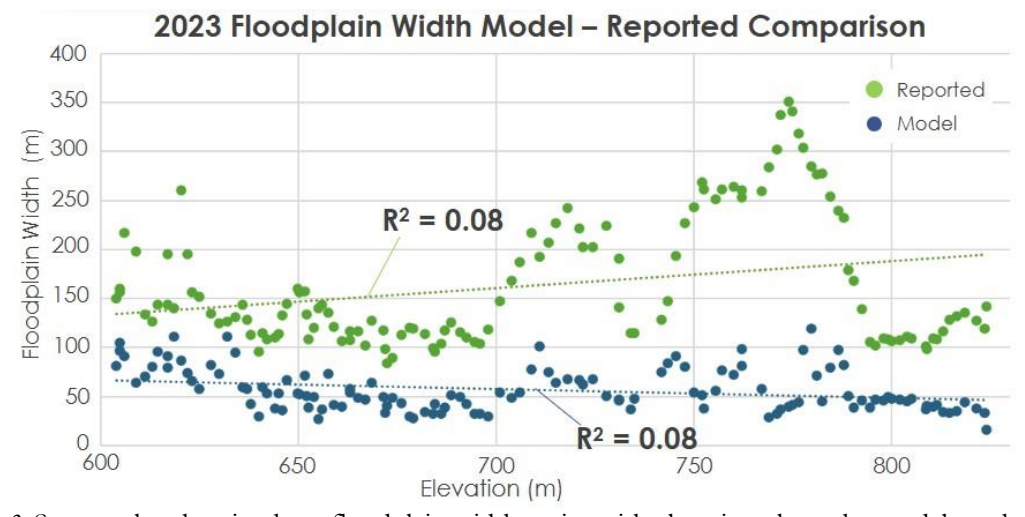


Figure 3. Scatter plot showing how floodplain width varies with elevation along the model reach for the reported (green) and modeled (blue) August 23, 2023, flood

#### 4.1.2 Backscatter Log Difference Maps from Sentinel-1 SAR

After calculating the log difference of backscatter values per pixel, our final output was a Backscatter Log Difference Map for the January 29, 2021 (Figure 4; Figure B1), and June 23, 2023, flood events (Figure B2). Water typically returns a weak backscatter value to the sensor due to its smooth surface, whereas surfaces with rougher features return a higher backscatter value (Hong et al., 2015). We presumed that blue pixels in the Log Difference Map are waterbodies or areas with standing flood water since these areas experienced a significant decrease in backscatter values between the pre- and post-flood dates. Areas showing increased backscatter values may be soil with higher moisture content or a result of the double-bounce effect. This phenomenon occurs when vertical features like urban buildings or vegetation intercept the return signal from waterbodies, and due to the side-looking nature of SAR sensors, results in higher backscatter value for water (Liao et al., 2020). There are additional steps that one can take to reduce the influence of the double-bounce effect from the results; however, we were limited to the 10-week project duration. The Log Difference Map for the June 2023 flood event showed more blue pixels, or areas of decreased backscatter, compared to the January 2021 result; however, the double-bounce effect is still evident. Vegetation seasonality or inundated vegetation could increase the backscatter value in the river corridor, and the magnitude and timing of the flood event could drive the greater change signals observed in the June flood event.

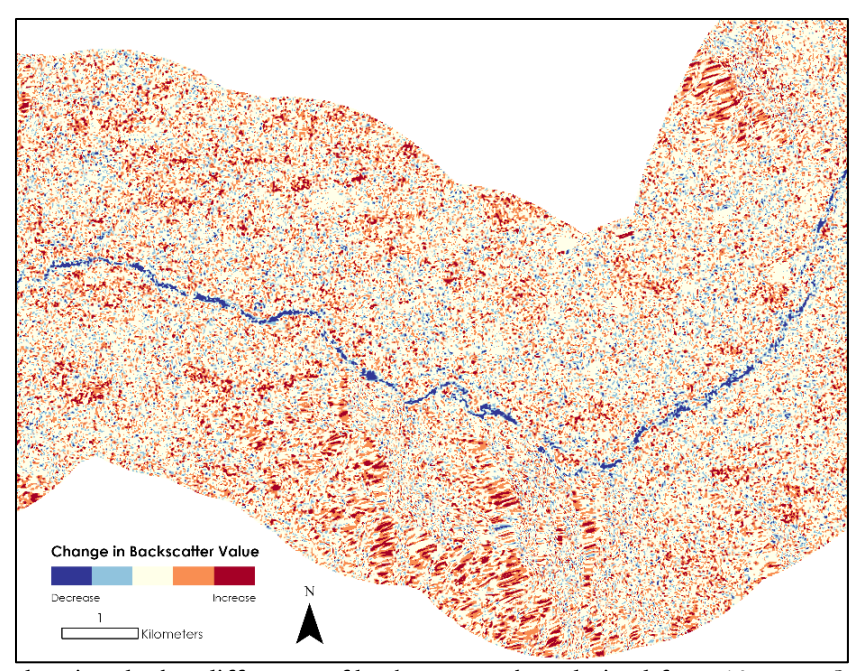


Figure 4: Map showing the log difference of backscatter values derived from 10-meter Sentinel-1 SAR datasets. Areas of increased backscatter are shown in red and decreased backscatter in blue between January 26, 2021, and February 1, 2021. The areas in dark blue are presumed to be standing water resulting from the flood.

#### 4.1.3 NDWI Difference Maps from Landsat and Sentinel-2

The results obtained from the NDWI calculation highlighted areas with significant changes in water content by comparing pre- and post-flood NDWI maps. NDWI values ranged from -1 to +1, with higher positive values (dark blue) indicating more water content. The comparison between pre- and post-flood NDWI maps for the August 2023 event revealed higher values in the NDWI, particularly in areas such as the Maipo River and urban regions, suggesting that these areas experienced prolonged wet conditions after the flood event (Figure 5).

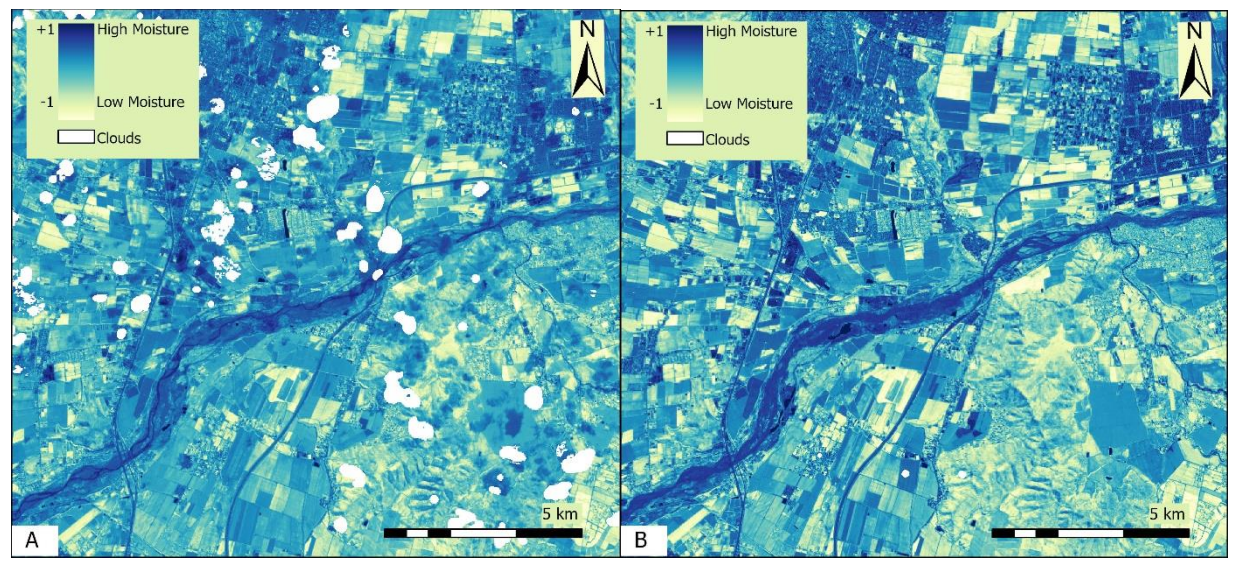


Figure 5. a) Pre-flood NDWI map (August 6) and b) post-flood NDWI map (August 26) for the August 2023 flood event, using Sentinel-2 MSI, 10-meter resolution imagery.

We observed similar results in the NDWI Difference Maps obtained from both Landsat 8-9 OLI and Sentinel-2 MSI (Figure C1). However, the NDWI Difference Map from Sentinel-2 showed a narrower range of NDWI values (from -1.1 to 1.2), while the map obtained from Landsat provided a wider NDWI range (from -1.6 to 1.2). These differences could be due to differences in spatial resolution between the sensors: Sentinel-2 MSI generally offers higher spatial resolution (10 meters) for key bands used in the NDWI calculation, such as band 3 and band 8, which are useful for monitoring vegetation health and agriculture. In contrast, Landsat 8 and Landsat 9 provide 30-meter resolution images and is best for assessing vegetation and land cover.

Another factor to consider is the different image capture dates used for the analysis. For example, the data from Sentinel-2 corresponds to the period of August 6 to August 26, 2023 while for Landsat, the images were taken from August 6 to August 30, 2023. This variation in the timing of the image captures could have influenced the NDWI change range, as the amount of standing water in the areas may have changed over time. Another factor that could have influenced the NDWI range is the presence of clouds and snow in the images and the atmospheric correction and cloud masking procedures applied.

#### 4.1.4 Comparison of Sentinel-2 MSI and Sentinel-1 SAR Flood Extent Maps

We compared the results of the NDWI Difference Map and Backscatter Log Difference Map over the confluence of the Maipo and Mapocho Rivers for the January 29, 2021 flood event (Figure D1). Sentinel-2 MSI and Sentinel-1 C-SAR offer a moderate 10-meter spatial resolution, providing similar levels of detail for observing the landscape. While both outputs allow us to see the river channel to some extent, the channel is more distinct in the NDWI Difference Map, while the Backscatter Log Difference Map has higher backscatter values along the uplands, likely due to wet soil and the double-bounce effect. Differences in flood detection between the sensors can be due to collection dates and sensor limitations. For example, Sentinel-2 MSI imagery is affected by cloud cover, which can obscure observations. In contrast, Sentinel-1 C-SAR can penetrate clouds, providing data regardless of weather conditions.

#### 4.2 Errors & Uncertainties

#### 4.2.1 HEC-RAS

We ran the HEC-RAS model using diffusion wave equations instead of full shallow water equations or full momentum. This choice involves removing parameters in exchange for shorter run times and improved model stability. By making this choice, the result is less accurate than one derived using full momentum.

The model also only has a single upstream boundary condition, and the topography does not change during the simulation. Our models did not account for additional tributary flows or surface runoff from the surrounding landscape. Additionally, the flows encountered for the flood events modeled are almost certainly erosive, resulting in the channel changing dynamically as the flood progressed. Dynamically modifying the underlying topo during a model run to get a more accurate floodplain extent is beyond the known capabilities of the HEC-RAS model. Finally, we did not account for several hydraulic control factors, namely bridges and dams. Because we did not have accurate measurements for these structures combined with the limited time frame to put these models together, bridges and dams along the model reach were not modeled. These structures would undoubtedly act as hydraulic controls, directly impacting how the floodplains are delineated.

#### 4.2.2 Sentinel-1 C-SAR

Using SAR to detect flood waters and surface water changes has limitations that could have impacted the accuracy of results. First, we found that the learning curve for SAR data processing was very steep, given the 10-week term of the project. We had difficulties processing the data in ArcGIS Pro because of licensing constraints, so we ultimately decided to process our imagery through the Alaska Satellite Facility's Data Search Portal. Regarding temporal resolution, we found that the return time of Sentinel-1 C-SAR did not always align with the dates of peak flooding, which affected data availability. Additionally, the time between image capture dates and peak flooding varied, which could have affected the analysis. While SAR's 10-m resolution shows detailed surface features, the spatial resolution may not be adequate to capture the river's geomorphology and the narrow size of the pre-flood river channels. Furthermore, topography influences the radar's return signal. For example, mountain slopes commonly cause shadowing and impact the brightness of features. Vertical features like vegetation, urban buildings, and mountains can influence the double-bounce effect, causing inaccurate sensor readings.

#### 4.2.3 NDWI from Landsat and Sentinel-2

The NDWI index is sensitive to the presence of vegetation, sediment loads and soil moisture. This sensitivity can result in misclassification of water bodies, especially in urban and densely vegetation areas. Additionally, spatial resolution of satellite images can lead to potential inconsistencies in water delineation. Lower resolution of imagery can reduce the ability to detect small water bodies. Furthermore, atmospheric conditions such as clouds, snow and seasonal variations can obscure water bodies and potentially impact the NDWI calculations.

#### 5. Conclusions

#### 5.1 Interpretation of Results

We resolved flood extents, evaluated flood trends with elevation, and compared methods using different sources of EOs for flood mapping in the Metropolitan Region. We found that hydraulic modeling is a feasible method for characterizing riverine floods when incorporating discharge observations from stream gauges. Hydraulic modeling can predict flood characteristics such as velocity, peak discharge, depth, and floodplain width. We analyzed these characteristics for different flood events (January 2021 and August 2023) and determined that the January 2021 extent was larger due to higher discharge. We compared the simulated floodplain widths with reported floodplain widths and found the HEC-RAS extents were consistently smaller. We determined that the hydraulic model's flood extent decreased with elevation, which contrasts with the reported floodplain trend.

Optical and radar datasets can also aid in flood extent analysis. By generating pre- and post-flood maps and calculating changes in NDWI and backscatter values, we identified areas of increased water within the floodplain, indicating inundation as opposed to permanent water bodies. We noticed distinct areas of standing water, particularly around the river, demonstrating that both NDWI and Log Difference calculations are effective in visualizing floods. However, these methods were prone to error. Challenges included a lack of available imagery around flood dates and the sensors' limited resolutions. The SAR imagery was prone to shadowing and the double-bounce effect, which can result in false positive areas of backscatter and decreased

detection of water. Due to these limitations, these products may be more suitable as supplemental materials rather than primary diagnostic tools for floodplain estimation.

## 5.2 Feasibility & Partner Implementation

We found hydraulic modeling to be a feasible method for predicting flood characteristics. CIREN can enhance the hydraulic model by incorporating local conditions and observations to improve the accuracy of their simulations. HEC-RAS allows for modeling bridges and culverts, adding in surfaces that represent soils and percent imperviousness, and supports grading the underlying topography to get a more accurate terrain, all of which would increase the accuracy of the model. Additionally, establishing more stream gauges and incorporating them into the model as boundary conditions would better capture tributary flows, resulting in more accurate flooding extents. CIREN could run their models using the full momentum equations for flow as opposed to the diffusion wave approach, which trades processing time for delineation accuracy.

HEC-RAS can potentially replace hand delineating floodplains in short order. We found that constructing a 2-D hydraulic model that captures the bulk flooding characteristics of an event can be accomplished in a few hours, while refining the model can take days to implement. Once the model is constructed, CIREN can quickly update it with the new discharge data as floods occur, run a diffusion wave simulation, and quickly produce a flooding extent for the event. This flooding extent can be readily exported from HEC-RAS as a shapefile for use in CIREN's other floodplain management workflows.

Both radar and optical data analysis are feasible methods for flood monitoring and assessment, with limitations. Accuracy may be affected by temporal limitations, cloud cover, snow, dense vegetation, topography, and backscatter effects. Due to these limitations, it may be more beneficial for our partners to use these methods as supplemental data for floodplain analysis, instead of basing floodplain extent from this data alone.

CIREN has experience with remote sensing methods, including SAR analysis. CIREN's remote sensing specialists can explore our methods and build upon them using local data. For example, if partners assess flood extents using the Log Difference in backscatter, they should consider the possibility of the double-bounce effect. To determine which areas are false positives due to double bounce, partners should cross-reference the Log Difference maps with land cover maps from the same time, which will allow them to identify areas with rough surfaces, indicating true increases in backscatter, and areas with vertical features such as vegetation and trees, indicating a potential double-bounce effect.

By adopting the hydraulic modeling and remote sensing techniques discussed herein, CIREN can better anticipate flood extent before floods happen and visualize those extents with high fidelity. These tools can be used together, allowing CIREN to further refine their understanding of the hydraulic characteristics in play that exacerbate flood damages within the Metropolitan Region. Additionally, these methods produce clear flooding visualizations that will help CIREN communicate flooding risks with their partners and the public. Future remote sensing and hydraulic modeling work performed by CIREN may generate new insights and lead to data-driven policies that protect Chileans, their property, and the region's natural resources.

## 6. Acknowledgements

We would like to extend our gratitude to our partners at CIREN and the Embassy of Chile's Agricultural Office, Carlos Calvo Cortés-Monroy, Vanessa Aros, Fernando Vasquez, Andres Rodriguez, and Adin Burwell. We also want to thank members of the Langley Research Center, including Dr. Kenton Ross (Science Advisor), Dr. Xia Cai (Science Advisor), Alyson Bergamini (Center Lead), and Brooklyn Appling (Geoinformatics Fellow). Additionally, we appreciate the guidance provided by Heidi Kristenson (Alaska Satellite Facility), James Milburn (ASF), Vinay Viswambharan (ESRI), and Lisa Tanh (ESRI). We appreciate all who contributed to the success of this project!

This material contains modified Copernicus Sentinel data (2021, 2023), processed by ESA.

Any opinions, findings, and conclusions or recommendations expressed in this material are those of the author(s) and do not necessarily reflect the views of the National Aeronautics and Space Administration.

This material is based upon work supported by NASA through contract 80LARC23FA024.

## 7. Glossary

ASF DAAC - Alaska Satellite Facility Distributed Active Archive Center

**Backscatter** - A measurement of the waves that reflect back to the satellite after it emits a signal **Double-Bounce Effect** – A phenomenon that occurs when a weak signal is reflected by water, but vertical features like urban buildings or vegetation intervene and "double-bounce" the original backscatter signal, resulting in a higher backscatter value

**Earth observations** – Satellites and sensors that collect information about the Earth's physical, chemical, and biological systems over space and time

**HEC-RAS-** Hydrologic Engineering Center's River Analysis System; used to create a two-dimensional hydraulic model of flood events

**Manning's** *n* – A parameter that represents the surface roughness associated with a given land cover type **NDWI** – Normalized Difference Water Index

NIR - Near Infrared band

**OLI** - Operational Land Imager

**RAS Mapper -** A GIS interface embedded within the HEC-RAS model, used for visualizing model results and constructing a two-dimensional model grid

RTC - Radiometric Terrain Correction

**SAR** – Synthetic Aperture Radar

Thalweg - the line or curve of lowest elevation within a watercourse, synonymous with channel centerline

#### 8. References

- Alaska Satellite Facility Distributed Active Archive Center. (n.d.). Sentinel-1 RTC Product Guide. ASF Hybrid Pluggable Processing Pipeline. <a href="https://hyp3-docs.asf.alaska.edu/guides/rtc\_product\_guide/">https://hyp3-docs.asf.alaska.edu/guides/rtc\_product\_guide/</a>
- Arab, S., Zelenak, D., Foga, S., and Hansen, T. (2024) Landsat Quality Assessment ArcGIS Toolbox. U.S. Geological Survey software release. <a href="https://doi.org/10.5066/P9HQISTY">https://doi.org/10.5066/P9HQISTY</a>
- Ban, H. J., Kwon, Y. J., Shin, H., Ryu, H. S., & Hong, S. (2017). Flood monitoring using satellite-based RGB composite imagery and refractive index retrieval in visible and near-infrared bands. *Remote Sensing*, 9(4). <a href="https://doi.org/10.3390/rs9040313">https://doi.org/10.3390/rs9040313</a>
- Casey, P., Willis, J., Silberman, Z., & Nelsen, S. (2022). Mexico Disasters: Comparing feasibility of flood detection methods using Google Earth Engine and Open Data Cube for flood mitigation in Mexico [Unpublished manuscript]. NASA DEVELOP National Program, Virginia Langley. https://ntrs.nasa.gov/citations/20220004584
- Chow, V.T. (1959). Open-Channel Hydraulics. Blackburn Press (Reprinted 2009).
- Copernicus Sentinel data [2021, 2023]. Retrieved from ASF DAAC [October 24, 2024], processed by ESA.
- Davies, R., (2023, August 22). *Chile Over 30,000 Evacuate Floods in 6 Regions*. News Report. <a href="https://floodlist.com/america/chile-floods-august-2023#:~:text=Disaster%20authorities%20in%20Chile%20report%20that%20over%2030%2C000,Chile%E2%80%99s%20second%20major%20flood%20event%20in%208%20weeks.
- Deutsche Welle (2024, June 14). *Chile hit by heavy rains, state of 'catastrophe' declared*. News Report. https://www.dw.com/en/chile-hit-by-heavy-rains-state-of-catastrophe-declared/a-69357808
- Earth Resources Observation and Science (EROS) Center. (2020). Landsat 8-9 Operational Land Imager / Thermal Infrared Sensor Level-2, Collection 2 [dataset]. U.S. Geological Survey. https://doi.org/10.5066/P9OGBGM6
- Ebert, A., Banzhaf, E., & McPhee, J. (2009). The influence of urban expansion on the flood hazard in Santiago de Chile. 2009 Urban Remote Sensing Joint Event. *IEEE*. <a href="https://doi.org/10.1109/URS.2009.5137601">https://doi.org/10.1109/URS.2009.5137601</a>
- Ebert, A., Welz, J., Heinrichs, D., Krelleneberg, K., & Hansjürgens, B. (2010). Socio-environmental change and flood risks: The case of Santiago de Chile. *ERDKUNDE*, *64*(4), 303–313. https://doi.org/10.3112/erdkunde.2010.04.01
- European Space Agency. (2015). Sentinel 2 Multispectral Imagery (MSI) / Level-2 Surface Reflectance [Dataset]. <a href="https://sentinels.copernicus.eu/web/sentinel/user-guides/sentinel-2-msi/processinglevels/level-2">https://sentinels.copernicus.eu/web/sentinel/user-guides/sentinel-2-msi/processinglevels/level-2</a>
- Gao, Bo-cai (1996). NDWI—A normalized difference water index for remote sensing of vegetation liquid water from space. Remote Sensing of Environment. 58(3), 257-266. https://doi.org/10.1016/S0034-4257(96)00067-3
- Gironás, J., Bunster, T., Chadwick, C., & Fernández, B. (2021). Floods. In B. Fernández & J. Gironás (Eds.), Water Resources of Chile, World water resources (Vol. 8). Springer. <a href="https://doi.org/10.1007/978-3-030-56901-3">https://doi.org/10.1007/978-3-030-56901-3</a>

- Hietpas, K., Ochoa-Madrid, E., Williams, E., & Spencer, O. (2021). Fairfax County Water Resources: Estimating Urban Flood Susceptibility, Historical Flooding Extent, and Land Cover Change in Fairfax County, Virginia to Aid in Flood Mitigation Planning [Unpublished manuscript]. NASA DEVELOP National Program, Virginia Langely. <a href="https://ntrs.nasa.gov/citations/20210011591">https://ntrs.nasa.gov/citations/20210011591</a>
- Hong, S., Jang, H., Kim, N., & Sohn, H.G. (2015). Water area extraction using RADARSAT SAR imagery combined with Landsat imagery and terrain information. *Sensors*, 15(3), 6652-6667. https://doi.org/10.3390/s150306652
- IFRC (2024, April 11). Chile: Floods June 2023 DREF Operation (MDRCL016) Final Report, Situation Report, International Federation of Red Cross and Red Crescent Societies.

  https://reliefweb.int/report/chile/chile-floods-june-2023-dref-operation-mdrcl016-final-report#:~:text=On%20June%2023rd,%20the%20impact%20intensified%20as%20communities%20 faced%20floods
- Kennedy, J. H., Smale, J., Johnston, A., Kristenson, H., Player, A., cirrusasf, Herrmann, J., Williams, F., Rine, J., & Logan, T. (2024, March 20). *ASFHyP3/asf-tools: ASF Tools v0.7.2* (Version v0.7.2) [Software]. Zenodo. <a href="https://doi.org/10.5281/zenodo.10845708">https://doi.org/10.5281/zenodo.10845708</a>
- Krellenberg, K., Muller, A., Schwarz, A., Hofer, R., & Welz, J. (2013). Flood and heat hazards in the Metropolitan Region of Santiago de Chile and the socio-economics of exposure. *Applied Geography*, *38*, 86-95. <a href="https://doi.org/10.1016/j.apgeog.2012.11.017">https://doi.org/10.1016/j.apgeog.2012.11.017</a>
- Kristenson, H. (2020, November 11). *RTC On Demand*! ArcGIS Story Map. https://storymaps.arcgis.com/stories/2ead3222d2294d1fae1d11d3f98d7c35
- Kristenson, H. (2020, November 17). *Log Difference Tool.* ArcGIS Story Map. https://storymaps.arcgis.com/stories/743d1126594b46e0b43be36473dba0e3
- Liao, H. & Wen, T. (2020). Extracting urban water bodies from high-resolution radar images: Measuring the urban surface morphology to control for radar's double-bounce effect. *International Journal of Applied Earth Observation and Geoinformation*, 85. https://doi.org/10.1016/j.jag.2019.102003
- Louis, J. (2021). Level-2A Algorithm Theoretical Basis Document. Ref. S2-PDGS-MPC-ATBD-L2A. European Space Agency. Issue 2.10. <a href="https://step.esa.int/thirdparties/sen2cor/2.10.0/docs/S2-PDGS-MPC-L2A-ATBD-V2.10.0.pdf">https://step.esa.int/thirdparties/sen2cor/2.10.0/docs/S2-PDGS-MPC-L2A-ATBD-V2.10.0.pdf</a>
- Luo T., Young, R., & Reig, P., (2015, August 26). Aqueduct Projected Water Stress Country Rankings. Technical Note. World Resources Institute, Washington, DC. <a href="https://www.wri.org/data/aqueduct-projected-water-stress-country-rankings">https://www.wri.org/data/aqueduct-projected-water-stress-country-rankings</a>
- Masek, J.G, Wulder, M, Markham, B., McCorkel, J., Crawford, C., Storey, J., & Jenstrom, D. (2020). Landsat 9: Empowering open science and applications through continuity. *Remote Sensing of Environment*, 248. https://doi.org/10.1016/j.rse.2020.111968
- McFeeters, S.K. (1996). The use of the Normalized Difference Water Index (NDWI) in the delineation of open water features. *International Journal of Remote Sensing*, 17(7), 1425-1432. https://doi.org/10.1080/01431169608948714

- Melancon, A.M., Molthan, A.L., Griffin, R.E., Mecikalski, J.R., Schultz, L.A., & Bell, J.R. (2021). Random forest classification of inundation following Hurricane Florence (2018) via L-band synthetic aperture radar and ancillary datasets. *Remote Sensing*, 13(24), 5098. https://doi.org/10.3390/rs13245098
- NASA JPL (2000). NASA Shuttle Radar Topography Mission Global 1 arc second. NASA EOSDIS Land Processing DAAC. Accessed [October, 2024]. https://doi.org/10.5067/MEaSUREs/SRTM/SRTMGL1.003
- Olivares, L., González, G., Matabenitez, G., Gironás, J., Viollier, E., Cienfuegos, R., Hora, B., Silva, J., Caravaca, L., Tironi, M., Campos-Knothe, K., García Martínez, Y., Ojeda Pereira, I., Martinez, C., Guerrero, N., Inzunza, S., Quense, J., Bonet, M., Merino, Y., & Concha, F. (2023). Inundaciones 21-26 Junio 2023 Cuencas del Río Mataquito y Río Maule (Región del Maule). *Informe Post Desastre, Inundaciones*, 21–26. <a href="https://doi.org/DOI:10.13140/RG.2.2.34718.10561">https://doi.org/DOI:10.13140/RG.2.2.34718.10561</a>
- Rojas, O., Mardones, M., Arumí, J.L., & Aguayo, M. (2014). Una revisión de inundaciones fluviales en Chile, período 1574–2012: causas, recurrencia y efectos geográficos. Revista de Geografía Norte Grande, 177–192. <a href="https://dx.doi.org/10.4067/S0718-34022014000100012">https://dx.doi.org/10.4067/S0718-34022014000100012</a>
- U.S. Army Corps of Engineers, Hydrologic Engineering Center (2024a). HEC-RAS Hydraulic Reference Manual. Version 6.6. <a href="https://www.hec.usace.army.mil/confluence/rasdocs/ras1dtechref/latest">https://www.hec.usace.army.mil/confluence/rasdocs/ras1dtechref/latest</a>
- U.S. Army Corps of Engineers, Hydrologic Engineering Center (2024b). Hydrologic Engineering Center's River Analysis System, Version 6.6. U.S. Army Corps of Engineers. <a href="https://www.hec.usace.army.mil/software/hec-ras/">https://www.hec.usace.army.mil/software/hec-ras/</a>.
- U.S. Geological Survey. Landsat 8 Operational Land Imager (OLI) Collection 2, Level 2, Tier 2 Surface Reflectance [Dataset]. Retrieved October 2024, from <a href="https://doi.org/10.5066/P9OGBGM6">https://doi.org/10.5066/P9OGBGM6</a>
- U.S. Geological Survey. Landsat Collection 2 Level 1 and Level 2 Quality Assessment (QA). Operational Land Imager (OLI) Collection 2, Level 2, Tier 2 Surface Reflectance [Dataset]. Retrieved October 2024, from <a href="https://www.usgs.gov/landsat-missions/landsat-collection-2-quality-assessment-bands#docs">https://www.usgs.gov/landsat-missions/landsat-collection-2-quality-assessment-bands#docs</a>
- Vicuña, S., Gironás, J., Meza, F.J., Cruzat, M.L., Jelinek, M., Bustos, E., Poblete D., & Bambach, M. (2013) Exploring possible connections between hydrological extreme events and climate change in central south Chile, *Hydrological Sciences Journal*, *58*(8), 1598-1619. https://doi.org/10.1080/02626667.2013.840380

## 9. Appendices

## Appendix A: Hydraulic Model

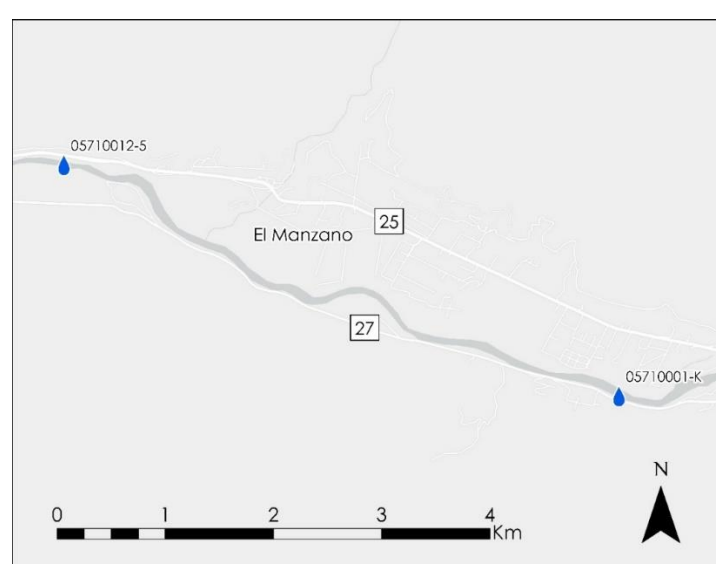


Figure A1. Location map of CIREN's stream gauges 05710012-5 and 05710001-K used in the HEC-RAS model. Basemap credits: Esri, TomTom, Garmin, Foursquare, METI/NASA, USGS

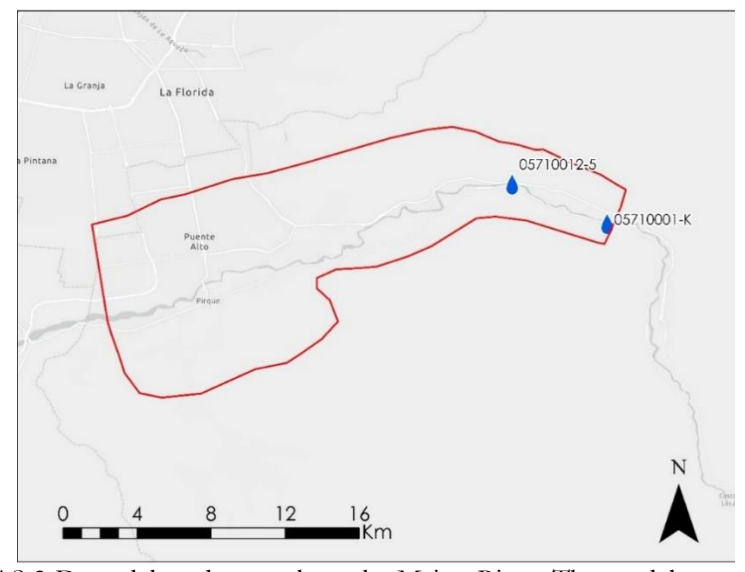


Figure A2. HEC-RAS 2-D model study area along the Maipo River. The model captured the river stretch between Highway 79 in the west and stream gauge 05710001-K in the east. Basemap credits: Esri, TomTom, Garmin, Foursquare, METI/NASA, USGS

Table A1
Temporal constraints set for the HEC-RAS model.

Flood Event	Date and Time (start)	Date and Time (end)	Computation Interval
January 29, 2021	January 27, 2021	February 1, 2021	5 seconds
	12:00am	6:00am	
August 23, 2023	August 18, 2023	August 24, 2023	5 seconds
	8:00 am	12:00am	

Table A2
Manning's n Values used in 2-D hydraulic model based on land cover data provided by CIREN.

CIREN Classification	Analog Manning's <i>n</i> Class (Chow, 1959)	Manning's n
Áreas Artificiales	Cement, Near Surface	0.011
Áreas Desprovistas de Vegetación	Excavated Channel, Earth Winding, No Vegetation	0.025
Bosques	Floodplain with Trees, Tree Stumps, Heavy Growth and Sprouts	0.06
Cuerpo de Agua	Water	0.02
Humedales	Floodplain, Pasture, No Brush, High Grass	0.035
Plantación Forestal	Floodplain, Trees, Cleared Land with Tree Stumps, No Sprouts	0.04
Praderas y Matorrales	Floodplain, Brush, Scattered Bursh, Heavy Weeds	0.05
Terreno Agrícola	Floodplain, Cultivated Areas, Mature Field Crops	0.04



Figure A3. Map of sampling points every 200 m along the Maipo River, Southeast of Santiago



Figure A4. Typical floodplain width comparison between the modeled (blue) August 23, 2023, floodplain extent and the reported (green) floodplain extent provided by CIREN

Table A3.

Summary of measured floodplain extent differences between the modeled August 23, 2023 floodplain and the reported floodplain provided by CIREN. Values obtained by subtracting the modeled width measurements from the reported measurements

Reported vs Modeled August 23, 2024 Floodplain Differences			
Maximum Difference (m)	310.5		
Minimum Difference (m)	15.4		
Average Difference (m)	106.4		

## Appendix B: Backscatter Difference Maps

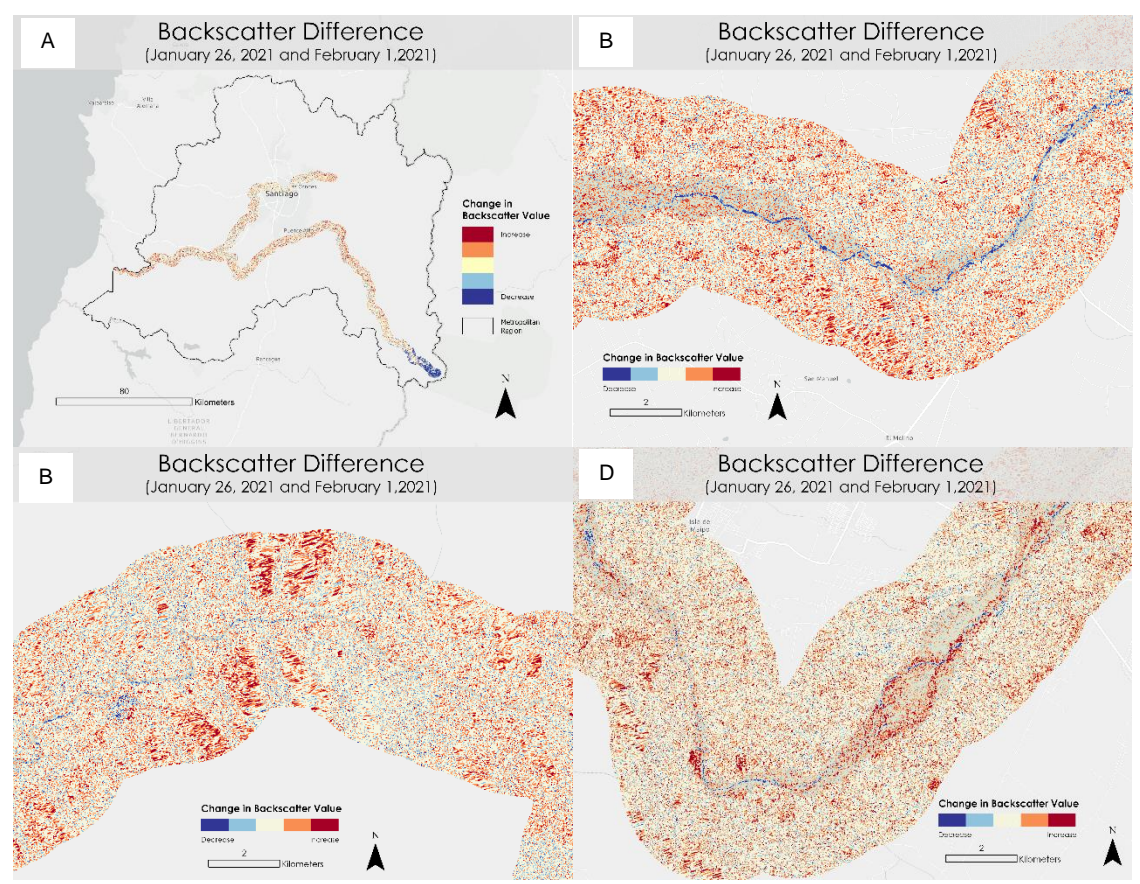


Figure B1: Map of the log difference in backscatter values across the Metropolitan Region (a) and stretches of the Maipo River (b, c, d). All images are representative of the January 29, 2021 flood event. Basemap credits: ESRI, TomTom, FAO, NOAA, USGS

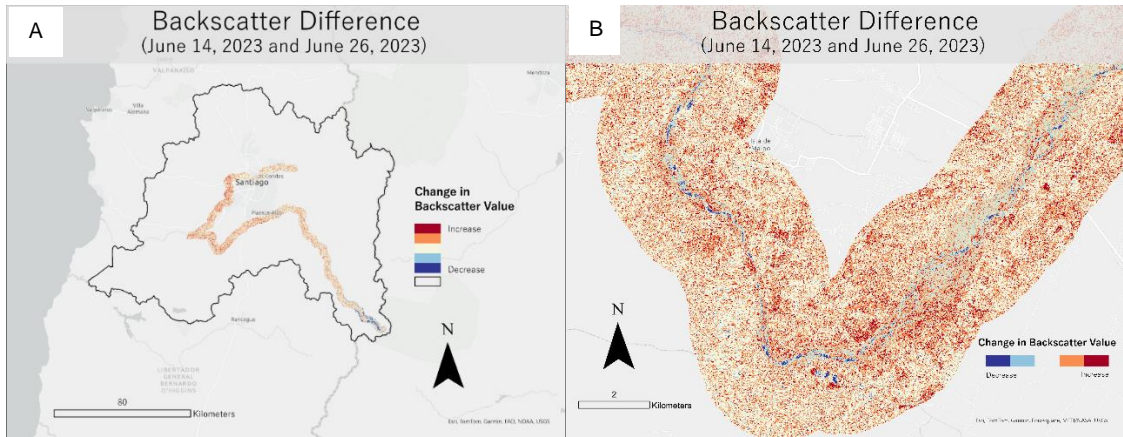


Figure B2. a.) Map of the Metropolitan Region and b.) Map of a curve of the Maipo River. Both images show the log difference in Sentinel-1 SAR backscatter values for the June 23, 2023 flood event. Basemap credits: ESRI, TomTom, FAO, NOAA, USGS

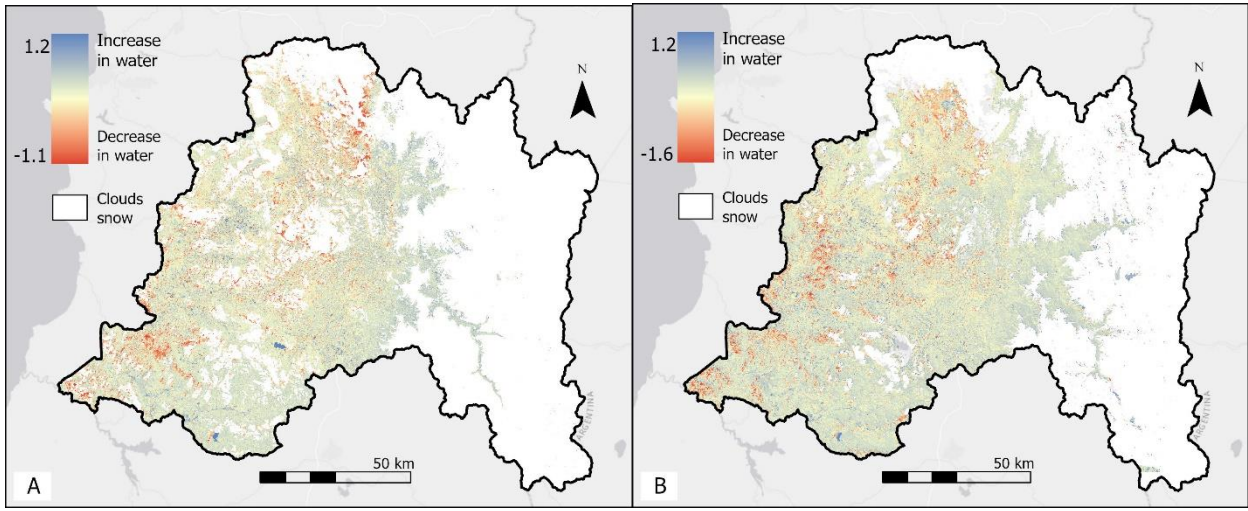


Figure C1: NDWI Difference Map using 10-meter Sentinel-2 MSI data (A) and NDWI Difference Map using 30-meter Landsat 8-9 data (B). Areas in blue indicate an increase in water content after the flood event, while areas in red shows decrease in water content. Basemap credits: Esri, HERE, Garmin, USGS

Appendix D: Maps Comparing Sentinel-2 MSI and Sentinel-1 SAR Methods For Visualizing Flooding

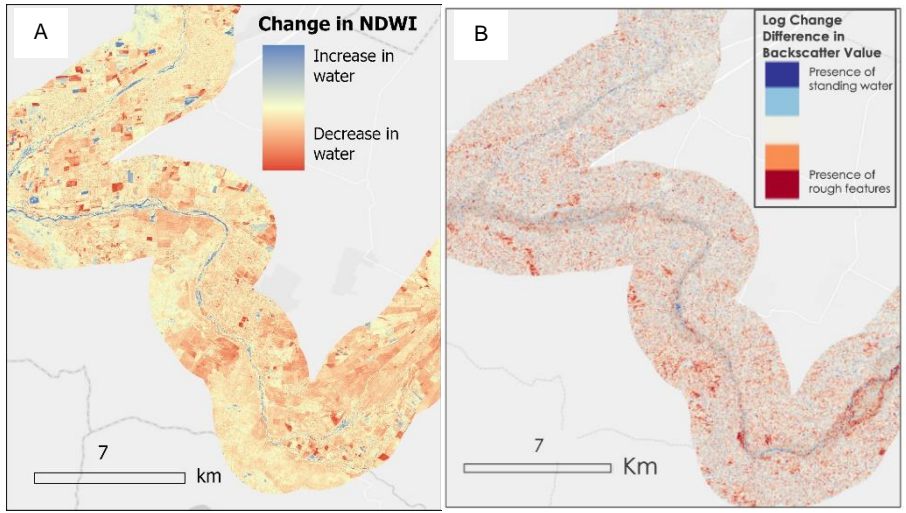


Figure D1: Map showing the change in NDWI values along the Maipo River, derived from Sentinel-2 MSI 10-meter imagery (A) and map showing the change in backscatter values, derived from Sentinel-1 SAR 10-meter imagery (B). In both figures, blue pixels indicate bodies of water. Basemap Credits: Esri, TomTom, Garmin, Foursquare, METI/NASA, USGS